ADVANCED OPTICAL MATERIALS
www.advopticalmat.de

Origin of the Unusual High Optical Nonlinearities Observed in Glassy Chalcogenides

*Jean-Baptiste Dory, Meryem Ibnoussina, Jean-Yves Raty, Jean-Baptiste Jager, Anthonin Verdy, Aurélien Coillet, Pierre Colman, Anthony Albanese, Martina Tomelleri, Benoit Cluzel, and Pierre Noé**

Nonlinear photonics integrated at the chip scale opens the path to new applications in an increasing number of fields such as all-optical computing, high bit rate communications on chip, or embedded sensing with frequency combs and super-continuum sources. All these applications require materials having the best trade-off between optical losses, Kerr refractive index, and compatibility with current nanofabrication facilities. Although optimizing the nanofabrication process can minimize linear optical losses to some extent, optimizing the Kerr index of the materials remains challenging because a clear understanding of the link between atomic structure and optical nonlinearities is still missing. This is precisely what this work addresses for chalcogenide glasses based on thin films of Ge-Sb-Se alloys, a promising class of materials fully compatible with large-scale integration technology from the microelectronics industry. By coupling nonlinear Kerr index metrology with ab initio molecular dynamics calculations of amorphous models, this work unveils the unique molecular patterns in these alloys that are responsible for their unusual nonlinear polarizability. This provides for the first time valuable rules for the design of new optical materials with improved Kerr index enabling miniaturization and implementation of future nonlinear photonic devices that can then operate at significantly lower power.

1. Introduction

Integrated nonlinear photonic devices are the ideal candidates for massive and on-chip deployment of advanced optical functions such as gas spectroscopy for environment and planetology, as well as clocks for metrology. More globally, these systems can also be key players for quantum and neuromorphic approaches for accelerated computing thanks to power consumption lower than that of older technologies.[1,2] The miniaturization and further reduction of total power consumption are nowadays limited by the optical nonlinearity of the materials. Indeed, the development of optical nonlinearities along a wave-guiding device scales with the nonlinear phase shift ($\Delta\phi$) accumulated by the light along its propagation axis: $\Delta\phi = \gamma PL$, where P is the power, L is the length, and γ the effective nonlinear parameter. This latter γ parameter includes contributions from the confinement of the optical field, which is directly related to the linear refractive index and the optical mode area (A_{eff}), and from the nonlinear polarizability of the material quantified by the material Kerr index (n_2). Thus, for the same total nonlinear effect, the higher the Kerr index, the smaller the device and the lower its operating power can be. For instance, fiber optics made of silica, which is the standard material for current optical telecommunications, exhibit a γ_{Silica} parameter in the 10^{-3} $(W.m)^{-1}$ range, coming from a combination of low linear and nonlinear indices. As a result, fiber-based

J.-B. Dory, J.-Y. Raty, A. Verdy, A. Albanese, M. Tomelleri, P. Noé
Université Grenoble Alpes
CEA
Leti
Grenoble F-38000, France
E-mail: pierre.noe@cea.fr

The ORCID identification number(s) for the author(s) of this article can be found under https://doi.org/10.1002/adom.202301154

DOI: 10.1002/adom.202301154

M. Ibnoussina, A. Coillet, P. Colman, B. Cluzel
ICB
UMR CNRS 6303
Université Bourgogne
Dijon cedex F-21078, France

J.-Y. Raty
Condensed Matter Simulation
CESAM
B5
Université de Liège
Sart-Tilman B4000, Belgium

J.-B. Jager
Université Grenoble Alpes
CEA
Grenoble INP
IRIG
PHELIQS
Grenoble F-38000, France

nonlinear photonic devices such as mode-locked fiber lasers, super-continuum sources, or optical clocks require long propagation lengths in the m-km range and intense optical power in the kW-MW range. This naturally prevents any onboard and miniaturized applications for such technology with reduced energetic fingerprints. On the other hand, materials coming from semiconductor technologies are very promising for building integrated nonlinear photonic devices since they exhibit high linear refractive index greater than 2 and Kerr indices in the 10^{-17}-10^{-19} $m^2.W^{-1}$ range, giving rise to γ as large as 10^2 $W^{-1}.m^{-1}$ for silicon, the golden material for microelectronics technologies. Five orders of magnitude separate the effective nonlinearities of silicon waveguides and silica fibers[3] emphasizing how meter-scale fiber-based systems could be miniaturized to a few micron device operating on a chip with only a few mW. To date, intense research efforts have been devoted to the development of such nonlinear photonic integrated devices. These efforts mainly stand on simply selecting material candidates being the most promising among the materials library from microelectronics and trying to find the best compromise to their limitations in terms of compatibility with complementary-metal-oxide-semiconductor (CMOS) technologies, nonlinear absorption losses, or transparency windows required for the final application.[4] To name just a few, III-V, IV-IV semiconductors, related oxides, and nitrides have been largely considered, but up to now, weak attention has been paid to the material optimization itself. Indeed, the Kerr index for a given material is considered as an intrinsic quantity without any possible optimization of it. Here, our approach follows the inverse direction. Ge-Sb-Se alloys are a promising class of glassy materials fully compatible with large-scale integration technology from microelectronic industry and with broad transparency windows and encouraging for applications in the visible wavelengths up to 12 μm in the mid-infrared (MIR). Besides, these chalcogenide glasses regain recently a huge interest since they were revealed as being prototypical Ovonic Threshold Switching (OTS) materials for use in selector devices that enabled recently the development of innovative 3D matrices of resistive memory cells through "cross-point" technology as nicely illustrated by the INTEL/MICRON OPTANE technology.[5] By choosing such a family of materials, we couple nonlinear Kerr index metrology and a state-of-the-art structural model derived from ab initio molecular dynamics (AIMD) calculations already validated by deep structural characterization, and we unveil the molecular motifs that are behind the uncommon high nonlinear polarizability of these alloys. Indeed, it is well admitted for a long time that glasses and amorphous materials exhibit a large variety of microscopic structures and molecular bonding that strongly depend on the elaboration method and considerably affect their overall physical properties. In nonlinear photonics, prior works on silicon-rich silicon nitride-based materials have shown that the higher the silicon ratio, the higher the Kerr index, until having a pure amorphous silicon layer that finally becomes unstable.[6] In this case, the rise of the optical nonlinearity may come with the increase of the amount of Si atoms and their related bonds having a higher polarizability than those made by the N ones. This emphasizes the critical role of atomic bonds in these materials onto their optical nonlinearities and this is precisely what motivates this work for understanding the link between these physical quantities. Here, we focus our attention on nonlinear Ge-Sb-Se glassy alloys because they provide a unique variety of chemical bonds and structural motifs with more or less (meta-)stability against aging or phase transformation. In particular, we reveal that structural motifs at origin of the huge nonlinearity responsible for the enhancement of the nonlinear refractive index of some specific Ge-Sb-Se compounds are reminiscent of the newly discovered "metavalent" bonds.[7,8] Finally, this work provides unique clues for designing at the atomic scale future nonlinear optical materials pushing further the miniaturization of nonlinear photonics and making it work at very low power.

2. Results

Chalcogenide materials are defined as non-oxide materials based on one of the elements of the column of O in the periodic table of elements. Most known and studied chalcogenides are based on S, Se, and Te elements. This materials family is very famous since their unique portfolio of properties is behind tremendous practical applications. They include in particular optic/photonic/THz applications,[10–15] phase-change memory or selector devices,[16] storage class memory and innovative neuromorphic circuits,[5,16–22] RF components,[23,24] photovoltaic cells,[25,26] thermoelectric devices,[27–29] emerging spintronic devices,[30,31] sensors[32–35] and so on. In this unique landscape, amorphous chalcogenide thin films based on the three chalcogen elements S, Se, and Te alloyed with Ge and Sb offer a unique playground to achieve a wide range of linear and nonlinear optical properties depending on composition.[12,36] More particularly, amorphous chalcogenides exhibit high linear refractive and Kerr indices, with huge variations depending on the composition. At this point, it is first instructive to display the optical properties of some of these materials on a map by comparison with other state-of-the-art materials for nonlinear optics. **Figure 1** shows the linear (n) and third-order nonlinear (n_2) refractive indices of prototypical nonlinear amorphous chalcogenide materials plotted with other highly nonlinear amorphous and crystalline materials. Crystalline materials, commonly used in numerous optical applications, exhibit a high polarizability,[37] but their crystalline state complicates fabrication by the need to match lattice parameters with the growth substrate. Non-chalcogenide amorphous compounds show either low polarizability as nitrides or oxides, or low stability as in case of a-Si.[38] However, excellent performances are reported in amorphous As-based chalcogenides.[39] Arsenic is a good chalcogenide glass former since it stabilizes the chalcogenide. However, As is known to easily form volatile harmful chemicals, imposing to implement restrictive measures during fabrication as well as all along the product's life. On opposite, Antimony, widely studied as an alloying element for electronic applications in phase-change materials such as $Ge_2Sb_2Te_5$ compound,[16] appears as a promising substitute to As in order to achieve very high linear and Kerr refractive indices in glassy chalcogenides.[40,41]

Figure 1 evidences also a trend between material bandgap, linear and nonlinear indices. Both indices significantly increase with the decrease of the bandgap energy of the material. In other words, as the bandgap energy of the material decreases, its electronic polarizability increases. However, even if this general trend is kept over the map, some slight discrepancies appear as for instance when comparing linear and nonlinear indices for

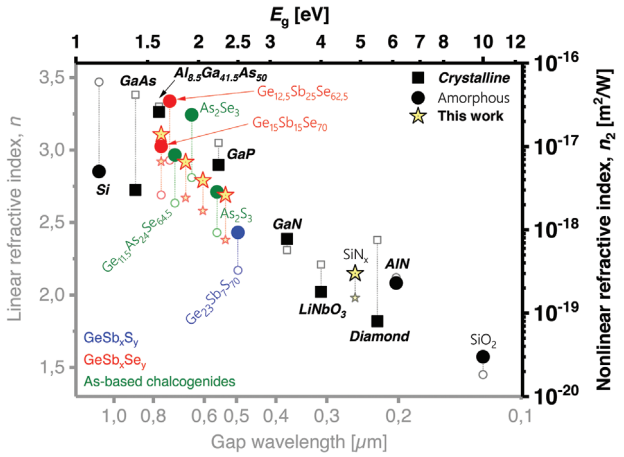

Figure 1. Plot of the linear (n) and nonlinear Kerr (n_2) refractive indices as well as bandgap energy E_g^{04} of amorphous chalcogenide compounds as well as those obtained on other classes of materials. Three different types of prototypical chalcogenides are distinguished here: Ge-Sb-S, Ge-Sb-Se, and As-based alloys. The values have been extracted from the literature[37,39,40] apart from those plotted with stars that correspond to some of our glassy Ge-Sb-Se-based alloys selected among all the chalcogenide films we studied and plotted in Figure 2 (for details see text and Experimental Section). The open and full symbols refer respectively for the same material to the linear and nonlinear index. The n values and the n_2 ones are those obtained at 1.55 μm (≈0.8 eV).

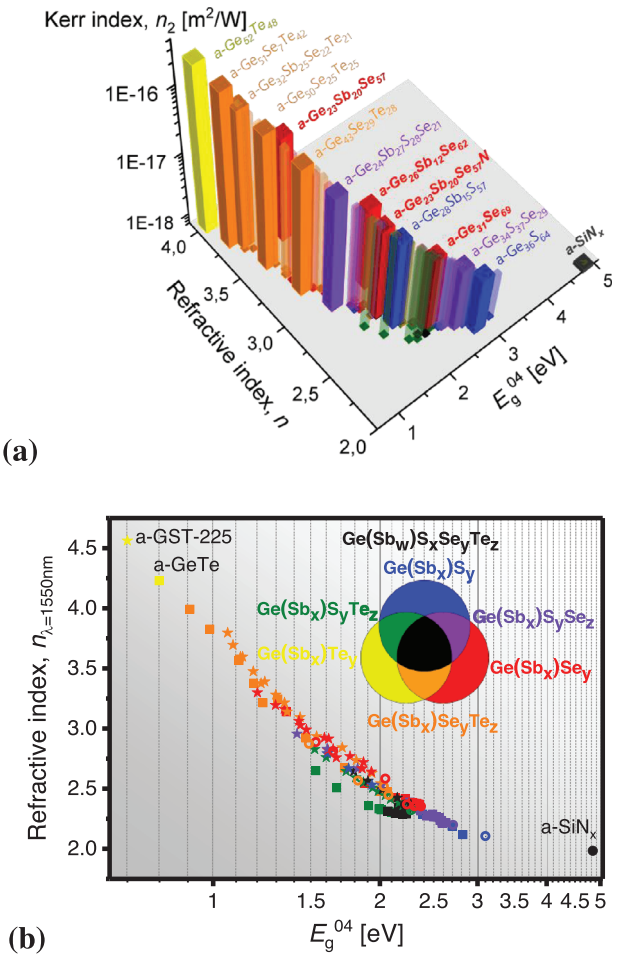

Figure 2. a) Plot of the linear (n) and maximal nonlinear Kerr (n_2) refractive indices at an energy of 0.534 x E_g^{04} as well as optical bandgap energy E_g^{04} as a function of compositions of amorphous Ge-Sb-S-Se-Te thin films obtained by (co-)sputtering. The linear optical constants (n and k) were obtained by modeling the spectroscopic ellipsometry data and were used to determine E_g^{04} and to calculate the maximal n_2 values using the Sheik-Bahae model (see the Experimental Section and reference [12]). b) Linear refractive index n at a wavelength of 1550 nm as a function of the bandgap energy E_g^{04} for the Ge-Sb-S-Se-Te thin films with a color map indicating the composition family from which belongs the data reported on the graph. The star, circle, and square symbols indicate the materials that contain Sb or N or neither, respectively.

the same material. For the same or close value of n, chalcogenide materials systematically exhibit a higher n_2 value compared with other materials. For instance, $Ge_{23}Sb_7S_{70}$ has an n value close to that of AlN but its n_2 is close to three times higher. The same applies also quite well when comparing GaP and $Ge_{12.5}Sb_{25}Se_{62.5}$ materials. Even if the n value of GaP is higher than that of the chalcogenide, the latter has an n_2 value close to six times that of GaP. Having said that it is evident that the origin of the surprising non-intuitive behavior of optical properties of chalcogenide materials deserves further investigation. To this aim, we studied a wide range of amorphous Ge-Sb-S-Se-Te chalcogenide compounds for which a systematic study of their linear and nonlinear optical properties has been performed. **Figure 2** gathers all the results obtained from this study on 85 amorphous chalcogenide thin films obtained by (co-)sputtering technique and more details are given in reference.[12] The n_2 values experience an exponential increase when going from $Ge_{36}S_{64}$ material toward $Ge_{52}Te_{48}$ one, which is one of the canonical compounds of phase-change materials. It is now well known that a huge jump of properties occurs when going from covalently-bonded GeS and GeSe crystals toward "metavalent" GeTe crystals.[42] This drop of properties in rhombohedral GeTe phase is characterized by a high chemical bond polarizability with unusually large Born effective charges, uncommon vibrational properties such as unusual phonon softening, and large Grüneisen parameters.[7,8] In GeTe and more generally in phase-change materials (PCMs), this has been ascribed very recently to the new metavalent bonding (MVB) mechanism that does not correspond to any of the previous mechanisms, namely ionic, covalent, resonant, or metallic bonding. MVB vanishes in the amorphous phase of GeTe and of all PCMs resulting from subtle structural changes at the local order in the material upon crystallization. This explains also their very fast phase transition. However, even if MVB is apparently destroyed in the amorphous phase of PCMs such as GeTe or $Ge_2Sb_2Te_5$ (GST 225), some reminiscence subsists in the glass as seen in Figure 2a,b showing the outstanding refractive indices of several of these amorphous chalcogenide materials and depending on their composition. Therefore, exploring the amorphous structure and the atomic bonding configuration in amorphous chalcogenides is the key to understanding the origin of their uncommon chemical bond polarizability and thus, nonlinear properties. This is what we explored hereafter using four different chalcogenide compounds: $Ge_{31}Se_{69}$, $Ge_{26}Sb_{12}Se_{62}$, $Ge_{23}Sb_{20}Se_{57}$, and N-doped $Ge_{23}Sb_{20}Se_{57}$. These alloys were chosen since they are prototypical compositions as well as the most promising for on-chip photonic applications due to their excellent trade-off

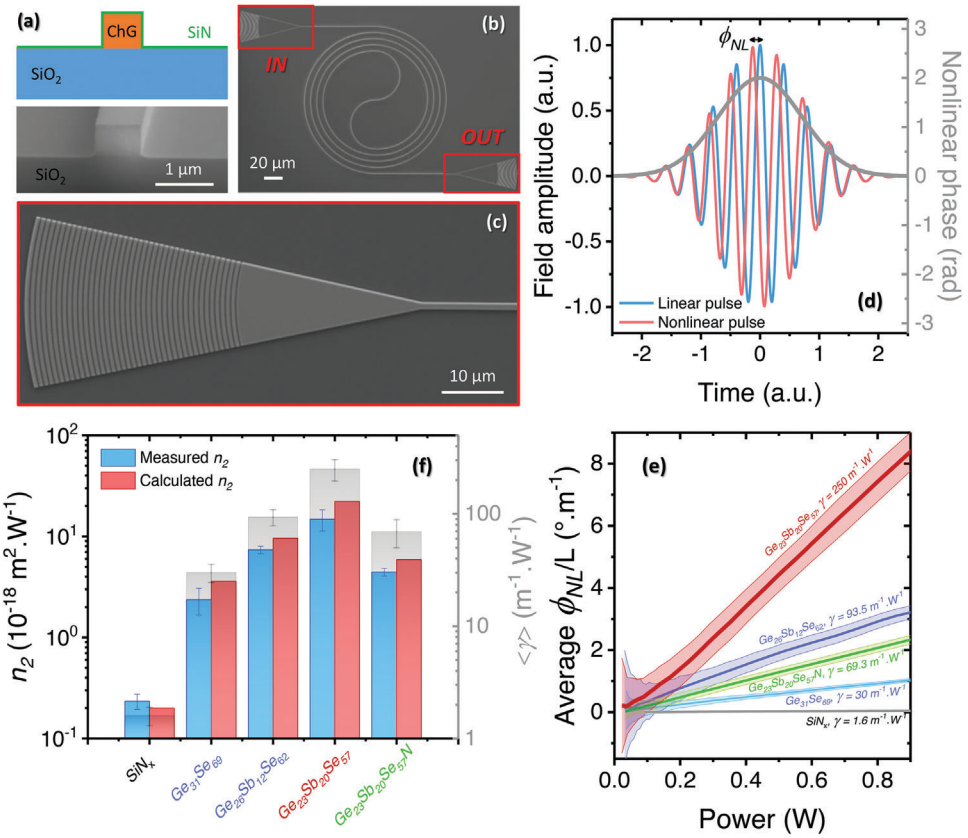

Figure 3. a) Schematic drawing, and scanning electron microscopy (SEM) image of the cross-section of a nonlinear chalcogenide waveguide ("ChG" on the drawing denotes the chalcogenide glass) fabricated in order to determine the nonlinear Kerr (n_2) refractive index of the material by means of heterodyne interferometry experiment as detailed in reference.[43] b) SEM image of the chalcogenide rib waveguides under test. For longer propagation length with a reduced footprint, the waveguide is shaped into an Archimedean spiral. c) SEM image showing the details of the input/output grating couplers (namely labeled "in" and "out" on (b)). Gratings are specifically designed for each material depending on its linear optical properties. d) Non-Linear Schrödinger Equation simulation of a nonlinear pulse showing the effect of the nonlinear phase-shift due to the Kerr effect. e) Measurement of the nonlinear phase shift after propagation through the nonlinear waveguide, depending on injected power. Total phase shift is normalized by the waveguide length; the linear slope is then the effective Kerr parameter of the waveguide. Colored areas denote the error bars. For comparison, typical results for silicon nitride SiN_x are also reported. f) Values of nonlinear Kerr (n_2) refractive index and nonlinear parameter γ at 1.55 µm obtained for four selected compositions of chalcogenide films as well as the SiN_x reference film. The n_2 values were calculated using the Sheik-Bahae model, and measured by means of nonlinear phase heterodyne interferometry experiment (see text). An excellent agreement is found between calculated and measured values of n_2 showing the huge increase of γ when going from SiN_x reference film toward $Ge_{23}Sb_{20}Se_{57}$ film.

between enough amorphous phase stability against crystallization, good infrared (IR) transparency, and high nonlinearity.[12]

Figure 3f shows the calculated and experimental values of nonlinear refractive index n_2 of the four chalcogenide compounds deposited by magnetron co-sputtering as detailed in reference.[12] For each material, the reported n_2 values were both calculated and measured experimentally. The calculated n_2 values were derived from the linear optical constants of the films determined by modeling of spectroscopic ellipsometry (SE) data acquired on the films using a Cody-Lorentz model (see Experimental Section). The measured n_2 values were determined by means of a nonlinear phase heterodyne interferometry experiment (for details on heterodyne technique see the Experimental Section and reference).[43] The effective nonlinear parameter $\gamma = 2\pi.n_2/(\lambda.A_{eff})$ is also reported for each material, with λ the wavelength and A_{eff}, the effective area of the optical mode propagating through the waveguide. For the sake of comparison and with the aim to validate the experimental procedure, both the calculated and experimental values of n_2 obtained on a SiN_x reference film were also plotted. As seen in Figure 3, within the error bars, the Kerr index of all materials are very similar in both calculated and experimental values. This demonstrates here that the used analytical model is well adapted to account for the nonlinear refractive index of thin films. Besides, as expected n_2 and γ are significantly higher in the Ge-Sb-Se-N chalcogenide films compared with SiN_x. The maximum is reached for the $Ge_{23}Sb_{20}Se_{57}$ film with a nonlinear parameter γ close to 250 $m^{-1}.W^{-1}$ which is >2 orders of magnitude higher than that of SiN_x ($\gamma \approx 1.6$ $m^{-1}.W^{-1}$). Such a value is highly promising for future nonlinear applications, moreover with a material that can be compatible with CMOS technology of microelectronic industry. Such a high nonlinear parameter γ is due to the unique chemical bonding and amorphous structure within such material and deserves further investigations to unveil the mechanism behind these uncommon optical properties for a glassy material.

3. Discussion

The Kerr indices of Ge-Sb-Se(-N) thin films are around one order of magnitude higher than that of the SiN_x reference. $Ge_{23}Sb_{20}Se_{57}N$ thin film has linear and Kerr refractive indices, as well as bandgap energy, lying in between those of $Ge_{26}Sb_{12}Se_{62}$ and $Ge_{31}Se_{69}$. It is worth noting that among the four selected chalcogenide films, only $Ge_{23}Sb_{20}Se_{57}N$, $Ge_{26}Sb_{12}Se_{62}$, and $Ge_{31}Se_{69}$ compounds exhibit a bandgap energy higher than 1.6 eV, corresponding to two-photon absorption (TPA) negligible at 1.55 µm (0.8 eV). For 1.55 µm applications based on propagation of non-linear optical effects and thus high optical energy, low TPA is a critical criterion to fulfill. However, $Ge_{23}Sb_{20}Se_{57}$ compound despite its highest TPA among the four selected compositions is the most suited for applications at wavelengths higher than 1.55 µm. Therefore, the $Ge_{23}Sb_{20}Se_{57}$ compound, with the highest nonlinearity among the compositions we studied here, is also a case study to explore the microscopic origin of the nonlinearity of chalcogenide glasses. The incorporation using two different concentrations of highly polarizable Sb atoms within $Ge_{31}Se_{69}$-based films permits to increase in the linear and nonlinear Kerr refractive indices and reduces the bandgap energy of the material, as demonstrated with $Ge_{26}Sb_{12}Se_{62}$ and $Ge_{23}Sb_{20}Se_{57}$ films.[12] As reported in previous works,[5,44] the incorporation of Sb atoms in $Ge_{30}Se_{70}$ leads to the formation of Sb-Sb "homopolar" and Ge-Sb "wrong" bonds, introducing undesired defect states in the bandgap of the material. As a result, these defect bonds are shown to have a major impact on the electronic properties of the film. This effect of Sb introduction is illustrated through a spectacular increase in refractive index mitigated by a significant increase of absorption in the near-infrared (NIR) due to a decrease of the bandgap energy.[12] The incorporation of N in these glasses is a key tool to prevent the formation of Sb-Sb "homopolar" and Ge-Sb "wrong" bonds, as well as improving the stability of the amorphous phase. This is very beneficial for selector applications since the introduction of N reduces subthreshold leakage currents while increasing the stability of the glass and thus the endurance of OTS devices.[5,44] However, as shown in Figure 3, N has the detrimental effect of reducing n_2.[44] Therefore, depending on the intended applications, a trade-off will have to be found between improving the stability of the amorphous and controlling the band gap of the material using N doping, for example with the aim of limiting losses such as two-photon absorption at the pump wavelength and increasing the polarizability by increasing the Sb concentration in the $Ge_{31}Se_{69}$ film.

Since we consider amorphous materials without any long-range order, these macroscopic changes in electronic and optical properties are only the result of a change in their local bonding configuration. In order to go further in the understanding, based on the careful structural characterization of the amorphous structure of chalcogenide thin films we built amorphous structural models for ab initio molecular dynamic (AIMD) simulations (see Sections 1 and 2 of the Supporting Information). **Figure 4**a shows a snapshot of the AIMD-simulated $Ge_{31}Se_{69}$ and $Ge_{23}Sb_{20}Se_{57}$ amorphous models (for details on simulations see the Experimental Section). The AIMD models were first validated on the basis of a detailed characterization of the amorphous structure of Ge-Sb-Se thin films performed by means of Raman, Fourier-Transform Infrared (FTIR), and X-ray Absorption Spectroscopies. An excellent agreement could be found between simulated models and experimental structure data.[5,12,44] Therefore, these relevant AIMD models are a unique tool in order to probe the physical properties of a material at a microscopic level. This is what we did in Figure 4a, in which we plotted the computed Born effective charges Z^* using Density Functional Perturbation Theory[45] of the Ge, Sb, and Se atoms for $Ge_{31}Se_{69}$, $Ge_{26}Sb_{12}Se_{62}$, $Ge_{23}Sb_{20}Se_{57}$ and $Ge_{23}Sb_{20}Se_{57}$ doped with N models. The Born effective charge Z^* characterizes the dynamic dipole moment that is created upon a vibronic displacement pattern. Hence, Z^* is a straightforward insight into the electronic polarizability of chemical bonds of a material as a function of the nature of its constitutive atomic elements.

As shown in Figures 2 and 3, the introduction of Sb in $Ge_{31}Se_{69}$ is at origin of the significant increase in the apparent macroscopic polarizability of the material. From an atomic-scale point of view, this is evidenced by formation of highly polarizable structural motifs around Sb atoms for which highest Z^* values are obtained. These highly polarizable motifs are those exhibiting Sb-Se bond angles close to 90° as well as the highest Sb coordination number up to 5. These patterns are not unlike those observed in the defective octahedra found in the amorphous phase of metavalent chalcogenide compounds such as GeTe or PbTe.[7,8] Surprisingly, the impact of Sb introduction in $Ge_{31}Se_{69}$ glass is not limited only to its local bonding. Indeed, the study of the average Z^* of the germanium atoms separately shows that the introduction of Sb in the $Ge_{31}Se_{69}$ model causes a significant increase of the polarizability by promoting the formation of distorted Ge tetrahedra with almost aligned bonds presenting higher polarizability (schematically represented in Figure 4b). It is worth noting that these quasi-aligned bonds are close to the highly polarizable bonds present in the crystalline phases of phase-change chalcogenide materials and are again defined as metavalent bonds. These metavalent bonds are at the origin of the very high polarizability of these phases resulting from a strong electronic delocalization.[5,7,8,44,46]

Similarly, Sb has also an impact on the polarizability of Se atoms as shown in Figure 4. The introduction of Sb increases the average Z^* of all selenium atoms. The increase in polarizability is more pronounced than for germanium atoms due to the appearance of highly polarizable Sb atoms in the vicinity of Se atoms. The Se atoms with the highest Z^* in the simulated $Ge_{31}Se_{69}$ (GS) and Sb-doped (12 and 20% at.) $Ge_{30}Se_{70}$ (GSS) models are those with an order parameter closest to 1. An order parameter close to 1 corresponds to Se atoms with a valence close to 3 (schematically represented in Figure 4b). The amount of these trivalent Se atoms increases with the introduction of Sb atoms in the $Ge_{31}Se_{69}$ model. Thus, the incorporation of Sb in the binary compound model $Ge_{31}Se_{69}$ increases the polarizability of the Se atoms by increasing the proportion of trivalent Se atoms, which are much more polarizable than bivalent selenium atoms. From the calculations, the effective polarization index is very similar for GSSN and GSS, with the differences being mainly in the distributions of the Z^* values and not in their average value, which affects n_2 in an unknown way. On the experimental side, however, it should be noted that the Kerr refractive index of the N-doped $Ge_{23}Sb_{20}Se_{57}$ film is smaller than that of the $Ge_{26}Sb_{12}Se_{62}$ film in Figure 3f. This is partly a result of the pumping wavelength of the heterodyne interferometry

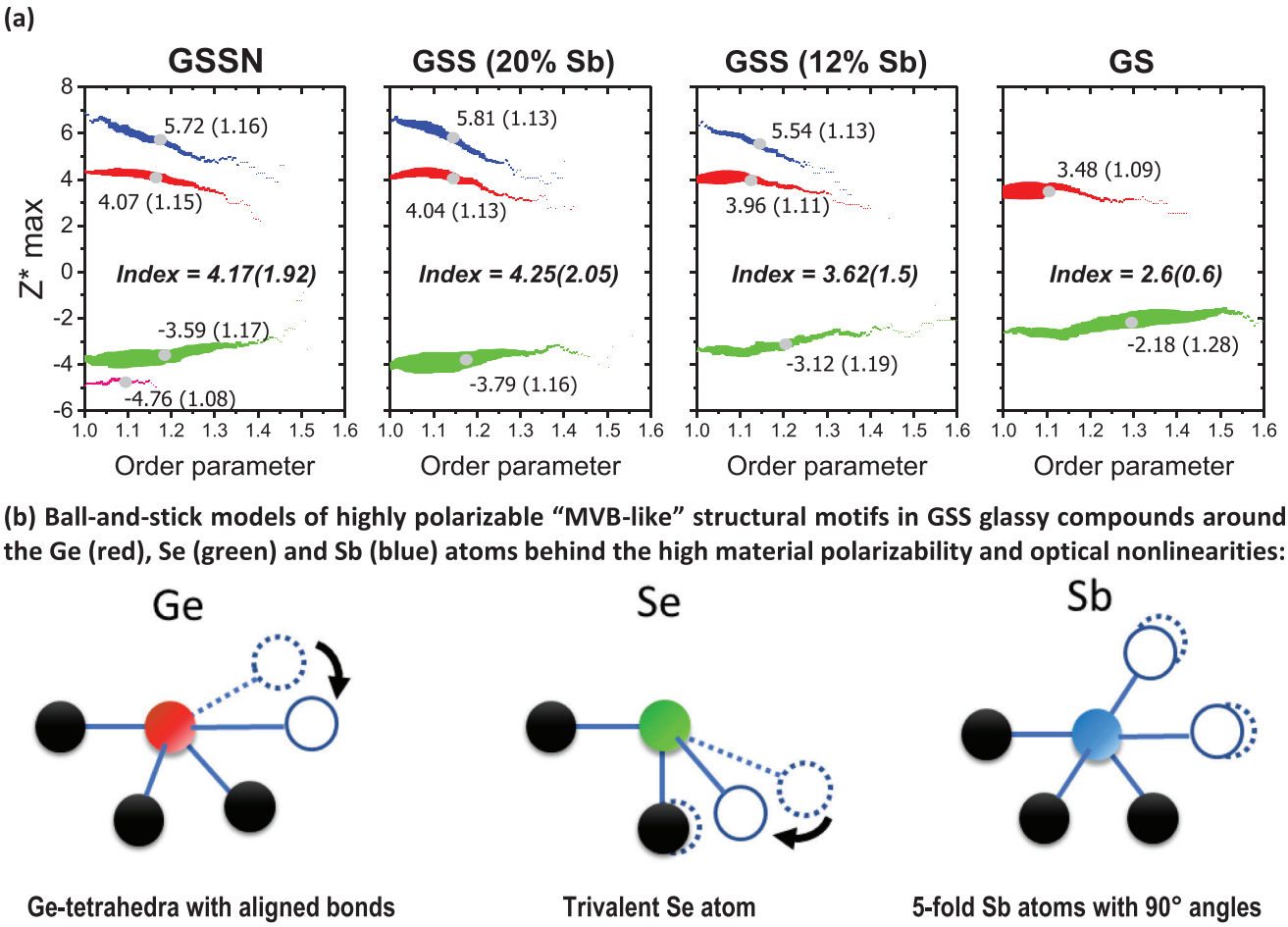

Figure 4. a) Dynamical charge for Ge (red), Se (green), Sb (blue), and N (pink) atoms in GS, GSS(12% Sb), GSS(20%Sb), and GSSN models, corresponding to $Ge_{31}Se_{69}$, $Ge_{26}Sb_{12}Se_{62}$, $Ge_{23}Sb_{20}Se_{57}$, and $Ge_{23}Sb_{20}Se_{57}$ doped with N chalcogenide glassy compounds. This is obtained through calculation of the Born effective charge Z^* for each of the atoms depending on their local bonding configuration distinguished using as *x*-axis of the order parameter. The latter represents the ratio of the fourth or third interatomic distance to the average of the first three or two distances for which typical structural motifs are shown in (b) (for details, see Experimental Section). The representation of the average Z^* value as a function of this order parameter allows to highlight the impact of the local order around the different atoms on their polarizability. The size of the symbol is proportional to the number of atoms standing in the same structural motif giving the same order parameter. A large increase in Z^* is observed for atoms that tend to have two aligned bonds (see the schematic structural motifs drawn in (b). For the Sb atoms, a significant increase of Sb bond polarizability occurs in motifs with a bond angle close to 90° recalling those observed in the crystalline phase of PCM exhibiting highly polarizable MVB bonds (see Figure S4 of the Supporting Information). The index values (the standard deviation from the latter are indicated in brackets) on each graph correspond to the calculated mean Z^* values (module) for all atoms in each model and are a representation of the overall material polarizability. The GSS(20%Sb) model exhibits the highest index among all materials explaining the very high Kerr and linear refractive indices measured experimentally in such compound as shown in Figure 3.

experiment to measure the n_2 values of the different materials. The Kerr refractive index n_2 peaks at a wavelength near 0.534 × E_g, where E_g is the band gap of the material.[12] As shown in the Tauc plots in Figure S6 of the Supporting Information, the N-doped $Ge_{23}Sb_{20}Se_{57}$ film has an optical band gap $E_g^{Ge23Sb20Se57\text{-}N}$ ≈1.9 eV different from that of the $Ge_{26}Sb_{12}Se_{62}$ film ($E_g^{Ge26Sb12Se62}$ ≈1.6 eV), so its n_2 value at 1.55 µm does not reach its maximum at 1.55 µm (≈0.8 eV). Therefore, although its calculated Z^* is higher than that of the $Ge_{26}Sb_{12}Se_{62}$ compound in Figure 4a, it should be noted that the Z^*_{max} measurement provides a rather qualitative view. Indeed, the "effective" polarization index we propose is slightly smaller for GSSN than for GSS. This should nevertheless not be over-interpreted.

To summarize, the peculiar structural motifs favored by introduction of Sb atoms in $Ge_{31}Se_{69}$ compound are responsible for the anomalies in dielectric properties observed in highly nonlinear amorphous Ge-Sb-Se films. Sb atoms generally form 2 long bonds and 2 short bonds with neighboring atoms. The presence of Sb atoms with valences up to 5 is also significant. The bond angles of the Sb atoms are ≈80 and 90°. The study of the average Z^* of antimony atoms as a function of bond angles shows that angles close to 90° correspond to more polarizable Sb atoms. As for Ge atoms, the bond alignment increases the polarizability of Sb atoms. The alignment of bonds around Ge and Sb atoms can be exalted under an electric field as described in a previous publication.[5] This alignment of bonds causes

the formation of patterns increasingly similar to the atomic arrangements observed in the crystalline phases of PCMs with metavalent bonds.[7,8] The formation of bonds close to the metavalent bonds at the origin of a strong local electron delocalization explains the outstanding polarizability of Se-based chalcogenide glass. This also explains the increase of polarizability when going from $Ge_{31}Se_{69}$ to $Ge_{23}Sb_{20}Se_{57}$. The incorporation of Sb promotes the presence of these aligned bonds hence increasing the polarizability of the chalcogenide compound by the incorporation of highly polarizable Sb, but also by modifying the structure of the amorphous and favoring the presence of strongly polarizable motifs.

Therefore, this novel insight opens numerous opportunities to develop novel chalcogenide glasses with improved polarizability for future nonlinear optical applications. The main limitation to the use of such bonds is the energy barrier for crystallization that tends to decrease when moving from purely covalently bonded glass, such as Ge-S compounds, toward the family of metavalently-bonded materials, such as Ge-Sb-Te PCM alloys.

To summarize, the relationship between composition and optical properties that we have described in this work is related to specific bonding characteristics. Indeed, the glasses with the highest n_2 values are those in which we found the highest proportion of highly polarizable atoms. It has been shown in the case of crystals that some compounds, which exhibit *p*-bonding with moderate ionicity, can have quasi-aligned bonds that are somehow electron-depleted bonds. These compounds do not obey the *8-N* rule ("octet rule") and the atoms are over-coordinated. They have been named as "metavalent" and are characterized by enhanced dielectric properties.[8,9] The present work shows that these effects can be present in a disordered medium in which highly polarizable atoms are over-coordinated. Therefore, other compositions could be studied to improve the optical properties, e.g. replacing Se by Te, Sb by Bi, or even Ge by Sn.

4. Conclusion

Amorphous chalcogenide thin films based on Ge-Sb-S-Se-Te exhibit promising nonlinear optical properties for bandgap energies between 0.8 and 2.8 eV. This range covers the energy range beyond 1.6 eV which corresponds to negligible two-photon absorption at 1550 nm in the material. The addition of Sb in Se-rich $Ge_{1-x}Se_x$ compounds is shown to increase the nonlinear Kerr refractive index n_2 moreover at a wavelength slightly higher than 1.5 μm that is of paramount interest for instance for 2 μm photonic applications. The increase of n_2 with addition of Sb is accompanied by an increase of the nonlinear parameter γ up to a value of ≈250 $m^{-1}.W^{-1}$ measured for the $G_{23}Sb_{20}Se_{57}$ thin film. This γ is more than 100 times higher than that obtained for the reference SiN film (≈1.6 $m^{-1}.W^{-1}$).

The study of the Born effective charge Z^* calculated from AIMD simulations of the $Ge_{31}Se_{69}$ and Sb-doped (12 and 20 at. %) $Ge_{30}Se_{70}$ models shows that the increase in polarizability related to the incorporation of Sb into the chalcogenide material is not solely the result of the higher polarizability of this element. Indeed, the addition of Sb has a beneficial effect on the local structure of the amorphous. Sb also induces the appearance of much more polarizable patterns resulting from the deformation of $GeSe_{4/2}$ germanium tetrahedra with two almost aligned bonds (forming angles close to 180°) as well as the increase of the proportion of trivalent selenium atoms. Regarding the Sb atoms, the most polarizable in the Sb-doped (12 and 20 at. %) $Ge_{30}Se_{70}$ compound models, they form bonds with angles close to 90° between them. The alignment of the bonds caused by the incorporation of Sb forms local order patterns with bond geometries reminiscent of the so-called metavalent bonds, as recently introduced to describe the crystalline phases of PCM chalcogenides. Increasing and controlling the proportion of these highly polarizable units in chalcogenide compounds is a promising route to engineer these materials aiming at further exalting their polarizability and thus their nonlinear properties. For instance, the realization of multilayer-type heterostructures by alternating deposition of nanoscale films of chalcogenide materials of different compositions would be a possible fabrication technique to force the formation of these highly polarizable patterns at the interfaces between the different layers while maintaining good thermal stability of the material with respect to crystallization.

Furthermore, the present results call for further studies related to the various current challenges for nonlinear photonics applications when using amorphous chalcogenides as nonlinear media.

First, the stability upon aging of amorphous chalcogenide has to be better understood. Since this depends on the composition of the material, this should be studied case by case by measuring, for instance, the change of optical properties upon aging at room temperature for a long time or by thermal aging after annealing below the glass transition temperature. This so-called "drift phenomenon" results from structural relaxation of the amorphous material.[16] This could be reversible only by heating the glass above its melting temperature and quenching of the molten phase Second, amorphous chalcogenides also differ from other materials in their uncommon photosensitivity related to photo-induced effects that could significantly affect their structure and properties. Photo-induced effects can lead to changes in band gap energy and refractive index. These effects, due to electron-hole (*e-h*) pairs generated by photon absorption in the amorphous semiconductor, can lead to, for example, increased photoconductivity (*e-h* splitting), photoluminescence (radiative *e-h* recombination), or photo-structural and optical changes (non-radiative *e-h* recombination).[47] Two classes of photo-induced effects in amorphous chalcogenides are distinguished based on the reversibility/irreversibility of property changes. Reversibility effects refer to effects that can induce a change in the amorphous that can be reversed back to the original properties. The recovery can be achieved by heating the material to a temperature close to the glass transition temperature T_g (metastable effects) or by stopping the illumination (transient effects). Irreversible effects, on the other hand, are permanent changes and the material can only be restored to its original properties by heating it above the T_g or melting temperature. Photo-darkening and photo-bleaching effects are light-induced effects specific to amorphous chalcogenides exposed to continuous-wave bandgap light or sub-bandgap light and appear within seconds or hours. In contrast, for illumination with nanosecond and ultrafast pulse lasers, transient absorption is most often observed on the picosecond to microsecond time scale. The latter could therefore affect the properties of the nonlinear amorphous chalcogenide film during intense optical pumping for NL applications. This should also be

studied in the future depending on the selected composition of the amorphous chalcogenide.

Finally, we believe that our conclusions are not restricted to Ge-Sb-Se alloys but could also be extended to other materials such as nitride, Arsenic based chalcogenides, or any other class of amorphous alloys involving the same type of bonds. This statement is well supported by recent demonstration of presence of a new "metavalent" bonding mechanism in halide perovskites that exhibit also huge optical nonlinearities.[9,48] As such, these results open a large avenue for developing new materials for nonlinear optics in which the microscopic structure could be engineered to maximize the Kerr index while preserving a stable amorphous phase and a broad transparency window.

5. Experimental Section

Chalcogenide Thin Film Deposition and Characterization: Details on the deposition conditions and determination of the linear and nonlinear optical properties of most of the chalcogenide films of the present manuscript were detailed in a previous reference.[12] It was noted that the deeply investigated GeSe-based chalcogenide thin films were deposited on 200/300 mm Si substrates in an industrial magnetron sputtering cluster tool using Ar as a plasma gas process. Sb-doped compositions were obtained by co-sputtering from pure Sb and $Ge_{30}Se_{70}$ targets. The incorporation of N in Ge-Sb-Se film was achieved by reactive co-sputtering of Sb and $Ge_{30}Se_{70}$ targets using an Ar/N_2 mixture in the sputtering plasma. Immediately after chalcogenide deposition, a 10 nm thick SiN_x or GeN_x capping layer was deposited in situ by reactive sputtering from a Si or Ge target under Ar/N_2 atmosphere to protect the chalcogenide films from oxidation. Wavelength Dispersive X-Ray Fluorescence (WDXRF) was used to control Ge, Sb, and Se contents of the films. A first set of samples with thicknesses of ≈100 nm and checked by X-ray Reflectivity was deposited for purpose of structural and optical characterization such as Raman, FTIR spectroscopies, and spectroscopic ellipsometry. For the other films composition of this work shown in Figure 1, all details were given in reference.[12]

A second set of thin film samples with same compositions had been deposited with thicknesses of ≈400–500 nm on a 3 µm thick thermal SiO_2 layer on top of the Si 200 mm substrate to permit fabrication of waveguiding structures required for experimental Kerr index determination by means of heterodyne experiment.

Spectroscopic Ellipsometry (SE) Measurements and Data Modeling: Spectroscopic ellipsometry measurements on the 100 nm thick films deposited on Si using a J. A. Woollam M-2000 equipment operating in the 190–1700 nm range was used to determine the real and imaginary parts of linear optical constants (refractive index *n* and extinction coefficient *k*) of the chalcogenide films as described in references.[5,12] SE data were collected at three incidence angles in range [55, 65, 70, and 75°] and the raw data were analyzed using WVASE 32 and CompleteEASE software. For ellipsometry data modeling, the SiN_x or GeN_x capping layers had been first measured and modeled separately to extract their optical constants, the latter being then injected in the model used for modeling of data acquired on the whole layers stacking. A Cody-Lorentz (CL) model was used to fit the experimental SE data and to extract linear optical constants of the chalcogenide films. Finally, the nonlinear Kerr indices of the films were also deduced from their linear optical constants by means of the Sheik-Bahae model as extensively described in a previous paper.[12]

Waveguides Fabrication and Nonlinear Refractive Index Measurement Using Heterodyne Interferometry Experiment: The SiN_x and chalcogenide waveguides were obtained by e-beam lithography (JEOL 6300FS) and plasma etching (OXFORD Plasmalab 100). A final 20 nm thick SiN_x capping layer was deposited to protect the chalcogenide waveguides from oxidation.

Then, the obtained SiN_x and chalcogenide waveguides were characterized by using a nonlinear phase heterodyne measurement setup as described in detail in reference.[43]

Ab initio Molecular Dynamic (AIMD) Simulations: The AIMD simulations were performed using the Vienna Ab Initio Software Package,[49] using PBESol exchange-correlation functional,[50] PAW potentials,[51,52] and 520 eV plane-waves cut-off. The 240 atoms structural models were obtained by performing simulated annealing using a melt-quench technique. The density was optimized at regular intervals during the quench to yield zero residual stress in the final amorphous structure. All systems were initially melted at fixed volume (experimental amorphous density) at 3000 K, and then progressively cooled down (1000 K-800 K-600 K-300 K). The cooling was performed in 30 ps. At each temperature plateau, the volume has been adjusted to minimize the stress, ensuring final residual stress that is typically smaller than 0.1 kbar.

Five independent trajectories had been generated for each system, using the PBESol functional, which had been shown to improve over regular PBE results for Ge-Sb-Te systems in the crystal phase,[53] without the need to add a van der Waals correction. All data presented had been obtained by averaging over 5 ps of trajectory at 300 K. The results on the structure of the simulated models were given in Supporting Information plotting the pair correlation function, the angle distribution, and the coordination numbers of atoms.

The response of the system to an electrical field had been characterized by the Born effective (dynamical) charge, that had been computed using linear response. The Born effective charges Z^* were computed using Density Functional Perturbation Theory.[45] The order parameter used to plot the fraction of Aligned Bond Pairs and the Born effective charge Z^* for Ge and Sb atoms was the ratio of the distance of an atom with the 4th closest atom, and the average of the distances with the three other closest atoms. A value of 1 was, in the case of Ge, obtained for a perfect tetrahedron, whereas a larger value was indicative of a threefold bonded atom, and intermediate values could be associated with distorted octahedra (as shown by the schematic structural motifs of Figure 4b). For instance, for Sb in $Ge_{23}Sb_{20}Se_{57}$, the average structure was a distorted octahedron, so that a value of 1 corresponded to an octahedron with four short distances and two longer ones. For Se atoms, the relevant order parameter was the ratio of the third distance to the average of the two shortest.

To measure the degree of anomalous response to an electrical field, a polarizability index was computed:

$$PI = 1/N \sum_i \left| Z_i^* - Z_{nom,\,i} \right| \quad (1)$$

with *i* designing the atoms, Z^* the effective charge and Z_{nom}, the nominal charge of the atom (Ge :+2 ; Sb :+3 ; Se :−2 ; N : −3).

Supporting Information

Supporting Information is available from the Wiley Online Library or from the author.

Acknowledgements

P.N. and B.C. acknowledge funding from the ANR (Agence Nationale de la Recherche) through OCTANE project (grant agreement ANR–20–CE24–0019). Nonlinear phase experiments were conducted on the facilities of the SMARTLIGHT platform funded by the ANR and Région Bourgogne Franche-Comté EQUIPEX + contract "ANR-21-ESRE-0040"). P.N. and B.C. also thank the French research group "GdR CHALCO", recently created for fruitful discussions (https://gdrchalco.cnrs.fr/). J.Y.R. acknowledges the FNRS CDR project ABIGLO (J.0154.21) as well as support from FNRS and computational resources provided by the CÉCI (funded by the F.R.S.-FNRS under Grant No. 2.5020.11) and the Tier-1 supercomputer of the Fédération Wallonie-Bruxelles (infrastructure funded by the Walloon Region under grant agreement n°1117545).

Conflict of Interest

The authors declare no conflict of interest.

Data Availability Statement

The data that support the findings of this study are available from the corresponding author upon reasonable request.

Keywords

AIMD, chalcogenide glass, Kerr refractive indexes, nonlinear optics, photonics

Received: May 17, 2023
Revised: June 1, 2023
Published online:

[1] S. M. Hendrickson, *J.OSA B Opt. Phys.* **2014**, *31*, 3193.
[2] R. S. Tucker, *IEEE* **2011**, *3*, 821.
[3] B. J. Eggleton, B. Luther-Davies, K. Richardson, *Nat. Photonics* **2011**, *5*, 141.
[4] M. Sieger, B. Mizaikoff, *Anal. Chem.* **2016**, *88*, 5562.
[5] P. Noé, A. Verdy, F. d'Acapito, J.-B. Dory, M. Bernard, G. Navarro, J.-B. Jager, J. Gaudin, J.-Y. Raty, *Sci. Adv.* **2020**, *6*, eaay2830.
[6] B.-U. Sohn, J. W. Choi, D. K. T. Ng, D. T. H. Tan, *Sci. Rep.* **2019**, *9*, 10364.
[7] J.-Y. Raty, M. Schumacher, P. Golub, V. L. Deringer, C. Gatti, M. Wuttig, *Adv. Mater.* **2019**, *31*, 1806280;
[8] M. Wuttig, V. L. Deringer, X. Gonze, C. Bichara, J.-Y. Raty, *Adv. Mater.* **2018**, *30*, 1803777.
[9] M. Wuttig, C.-F. Schön, M. Schumacher, J. Robertson, P. Golub, E. Bousquet, C. Gatti, J.-Y. Raty, *Adv. Funct. Mater.* **2022**, *32*, 2110166.
[10] P. Martinez, I. Papagiannouli, D. Descamps, S. Petit, J. Marthelot, A. Lévy, B. Fabre, J.-B. Dory, N. Bernier, J.-Y. Raty, P. Noé, J. Gaudin, *Adv. Mater.* **2020**, *32*, 2003032.
[11] J. Wang, L. Wang, J. Liu, *IEEE Access* **2020**, *8*, 121211.
[12] J.-B. Dory, C. Castro-Chavarria, A. Verdy, J.-B. Jager, M. Bernard, C. Sabbione, M. Tessaire, J.-M. Fédéli, A. Coillet, B. Cluzel, P. Noé, *Sci. Rep.* **2020**, *10*, 11894.
[13] J. Lemaitre, A. Gutierrez, E. Delcourt, W. El Ayed, P. Pirasteh, L. Bodiou, Y. Dumeige, I. Hardy, J. Charrier, E. Baudet, F. Starecki, R. Chahal, M. Baillieul, V. Nazabal, in *19th European Conference on Integrated Optics (ECIO 2017)*, **2017**.
[14] M. Wuttig, H. Bhaskaran, T. Taubner, *Nat. Photonics* **2017**, *11*, 465.
[15] P. Pitchappa, A. Kumar, S. Prakash, H. Jani, T. Venkatesan, R. Singh, *Adv. Mater.* **2019**, *31*, 1808157.
[16] P. Noé, C. Vallée, F. Hippert, F. Fillot, J.-Y. Raty, *Semicond. Sci. Technol.* **2018**, *33*, 013002.
[17] P. Fantini, *J. Phys. D: Appl. Phys.* **2020**, *53*, 283002.
[18] P. Cappelletti, R. Annunziata, F. Arnaud, F. Disegni, A. Maurelli, P. Zuliani, *J. Phys. D: Appl. Phys.* **2020**, *53*, 193002.
[19] M. Le Gallo, A. Sebastian, *J. Phys. D: Appl. Phys.* **2020**, *53*, 213002.
[20] T. Kim, S. Lee, *IEEE Trans. Electron Devices* **2020**, *67*, 1394.
[21] M. Xu, X. Mai, J. Lin, W. Zhang, Y. Li, Y. He, H. Tong, X. Hou, P. Zhou, X. Miao, *Adv. Funct. Mater.* **2020**, *30*, 2003419.
[22] P. Noé, B. J. Kooi, M. Wuttig, *physica status solidi (RRL) – Rapid Research Letters* **2021**, *15*, 2100078.
[23] R. M. Young, P. Borodulin, N. El-Hinnawy, A. Ezis, M. R. King, V. Luu, D. T. Nichols, in *2018 IEEE/MTT-S International Microwave Symposium – IMS*, **2018**, 832–835.
[24] M. Wang, M. Rais-Zadeh, *J. Micromech. Microeng.* **2017**, *27*, 013001.
[25] S. Ishizuka, P. J. Fons, *ACS Appl. Mater. Interfaces* **2020**, *12*, 25058.
[26] S.-C. Liu, Y. Mi, D.-J. Xue, Y.-X. Chen, C. He, X. Liu, J.-S. Hu, L.-J. Wan, *Adv. Electron. Mater.* **2017**, *3*, 1700141.
[27] D. Wu, L. Xie, X. Xu, J. He, *Adv. Funct. Mater.* **2019**, *29*, 1806613.
[28] J. Wang, C. Zhou, Y. Yu, Y. Zhou, L. Lu, B. Ge, Y. Cheng, C.-L. Jia, R. Mazzarello, Z. Shi, M. Wuttig, W. Zhang, *Nano Energy* **2021**, *79*, 105484.
[29] C. Rodenkirchen, M. Cagnoni, S. Jakobs, Y. Cheng, J. Keutgen, Y. Yu, M. Wuttig, O. Cojocaru-Mirédin, *Adv. Funct. Mater.* **2020**, *30*, 1910039.
[30] J. Reindl, H. Volker, N. P. Breznay, M. Wuttig, *npj Quantum Mater.* **2019**, *4*, 57.
[31] S. Varotto, L. Nessi, S. Cecchi, J. Sławińska, P. Noël, S. Petrò, F. Fagiani, A. Novati, M. Cantoni, D. Petti, E. Albisetti, M. Costa, R. Calarco, M. Buongiorno Nardelli, M. Bibes, S. Picozzi, J.-P. Attané, L. Vila, R. Bertacco, C. Rinaldi, *Nat Electron* **2021**, *4*, 740.
[32] P. Su, Z. Han, D. Kita, P. Becla, H. Lin, S. Deckoff-Jones, K. Richardson, L. C. Kimerling, J. Hu, A. Agarwal, *Appl. Phys. Lett.* **2019**, *114*, 051103.
[33] K. V. Sreekanth, Q. Ouyang, S. Sreejith, S. Zeng, W. Lishu, E. Ilker, W. Dong, M. El Kabbash, Y. Ting, C. T. Lim, M. Hinczewski, G. Strangi, K. Yong, R. E. Simpson, R. Singh, *Adv. Opt. Mater.* **2019**, *1900081*, 1900081.
[34] E. Baudet, M. Sergent, P. Němec, C. Cardinaud, E. Rinnert, K. Michel, L. Jouany, B. Bureau, V. Nazabal, *Sci. Rep.* **2017**, *7*, 3500.
[35] M.-L. Anne, J. Keirsse, V. Nazabal, K. Hyodo, S. Inoue, C. Boussard-Pledel, H. Lhermite, J. Charrier, K. Yanakata, O. Loreal, J. Le Person, F. Colas, C. Compère, B. Bureau, *Sensors (Basel, Switzerland)* **2009**, *9*, 7398.
[36] Z. Yang, Z. Yang, R. Zhang, R. Zhang, Z. Wang, Z. Wang, P. Xu, P. Xu, P. Xu, W. Zhang, W. Zhang, W. Zhang, Z. Kang, Z. Kang, J. Zheng, S. Dai, S. Dai, R. Wang, R. Wang, R. Wang, A. Majumdar, A. Majumdar, *Opt. Express OE* **2021**, *29*, 33225.
[37] D. J. Wilson, K. Schneider, S. Hönl, M. Anderson, Y. Baumgartner, L. Czornomaz, T. J. Kippenberg, P. Seidler, *Nat. Photonics* **2020**, *14*, 57.
[38] H. A. Bosan, W. Beyer, U. Breuer, F. Finger, N. Hambach, M. Nuys, F. Pennartz, D. Amkreutz, S. Haas, *Phys. Status Solidi A* **2021**, *218*, 2000435.
[39] T. Wang, X. Gai, W. Wei, R. Wang, Z. Yang, X. Shen, S. Madden, B. Luther-Davies, *Opt. Mater. Express* **2014**, *4*, 1011.
[40] T. Kuriakose, E. Baudet, T. Halenkovic, M. M. R. Elsawy, P. Nemec, V. Nazabal, G. Renversez, M. Chauvet, *Opt. Commun.* **2017**, *403*, 352.
[41] S. Serna, H. Lin, C. Alonso-Ramos, A. Yadav, X. Le Roux, K. Rihardson, E. Cassan, N. Dubreuil, J. Hu, L. Vivien, *Photonics Res* **2018**, *6*, B37.
[42] J.-Y. Raty, M. Wuttig, *J. Phys. D: Appl. Phys.* **2020**, *53*, 234002.
[43] M. Ibnoussina, A. Coillet, J.-B. Dory, J.-B. Jager, P. Colman, P. Noé, B. Cluzel, *Opt. Lett.* **2020**, *45*, 5053.
[44] A. Verdy, F. d'Acapito, J.-B. Dory, G. Navarro, M. Bernard, P. Noé, *physica status solidi (RRL) – Rapid Research Letters* **2020**, *14*, 1900548.
[45] X. Gonze, C. Lee, *Phys. Rev. B* **1997**, *55*, 10355.
[46] J.-Y. Raty, P. Noé, *physica status solidi (RRL) – Rapid Research Letters* **2020**, *14*, 2070024.
[47] P. Khan, K. V. Adarsh, *Physics* **2021**, *3*, 255.
[48] J. Xu, X. Li, J. Xiong, C. Yuan, S. Semin, T. Rasing, X.-H. Bu, *Adv. Mater.* **2020**, *32*, 1806736.
[49] G. Kresse, J. Hafner, *Phys. Rev. B* **1994**, *49*, 14251.
[50] J. P. Perdew, K. Burke, M. Ernzerhof, *Phys. Rev. Lett.* **1996**, *77*, 3865.
[51] G. Kresse, D. Joubert, *Phys. Rev. B* **1999**, *59*, 1758.
[52] P. E. Blöchl, *Phys. Rev. B* **1994**, *50*, 17953.
[53] W. Ibarra-Hernández, J.-Y. Raty, *Phys. Rev. B* **2018**, *97*, 245205.